Denoising of Brillouin Gain Spectrum Images for Improved Dynamic Measurements of BOTDR

Bo Li ©, Ningjun Jiang ©, and Xiaole Han ©

Abstract—Brillouin optical time-domain reflectometry (BOTDR) is widely used for strain and temperature measurements in various fields. However, the accuracy and reliability of the measurements are often limited by the noise in the sensor signals. Dynamic measurement of BOTDR requires small averaging number and fast measurement, and hence noise reduction is more significant in dynamic measurement. Small gain stimulated Brillouin scattering (SBS) can enhance the Brillouin signal power in BOTDR to realize dynamic measurement, but noise reduction is still important in system. In this work, we investigate the denoising of Brillouin gain spectrum (BGS) images using convolutional neural networks (DnCNN) to improve the accuracy of the small gain SBS STFT-BOTDR measurement of strain vibration. It is shown that the denoising of BGS images along the time axis can result in better detection of the strain vibration compared with denoising of BGS images along the fiber length. The denoising performance was evaluated using frequency uncertainties and R-squared values. The best denoising performance was achieved with a DnCNN network with 8 layers and 200 epochs, leading to a frequency uncertainty of 2.32 MHz and an R-squared value of 0.907. The frequency uncertainty is improved to about 45% of the original value.

Index Terms—Brillouin optical time-domain reflectometry, deep learning, distributed fiber optic sensors, image denoising.

I. INTRODUCTION

THE Brillouin scattering based distributed fibre optic sensors have the advantages of distributed measurement of the temperature and strain information along the optic fibre, which are crucial indicators in structural health monitoring [1]. Thanks to the benefits of small in size, stable in harsh environments and easy installation, distributed fibre optic sensors are more and more widely used in fields such as oil and gas industries, bridge monitoring, and power plant and building monitoring [2]. Apart from the static sensing, vibration sensing is another important topic in the monitoring of structures, such as the earthquake alarm and inspections in aeronautics industry. Cracks and breaks are found from many aging structures that were designed to be quake-proof. Without proper monitoring, these damages can only be recognized by visual inspections which lacks immediate assessment [3].

The Brillouin optical time domain analysis (BOTDA) and the Brillouin optical time domain reflectometry (BOTDR) are the two major classes of the Brillouin scattering based distributed fibre optic sensors [4]. As access to only one end of the optic fibre is needed with BOTDR, it is more maneuverable and preferred in practical applications [5]. However, as the power of the spontaneous Brillouin scattering in the optic fibre is very weak, large number of averaging is required in the BOTDR system to reduce the noise and increase the signal-to-noise ratio (SNR), which demands long sensing time and limits the speed of the measurement and hence makes it difficult for dynamic sensing of vibrations. Targeting at the desired sensing length of around 1km for civil engineering applications, dynamic measurement of the BOTDR system is realized by inducing small gain stimulated Brillouin scattering (SBS) together with short time Fourier transform (STFT) [6]. The signal power is boosted with small gain SBS, but more noise is maintained since the averaging number is small. To further improve the output performance of this small gain SBS STFT-BOTDR, noise reduction is needed.

The strain and temperature information is represented by Brillouin frequency shift (BFS), which is derived as the center frequency of the Brillouin gain spectrum (BGS). By conducting STFT on the captured time domain data from the system, BGS information can be obtained. Hence, denoising of the BGS can enhance the accuracy of BFS detection.

By treating the BGSs along the FUT as a two-dimensional image, image denoising methods such as non-local means (NLM), wavelet denoising (WD), and block-matching and 3D filtering (BM3D) have been used on Brillouin based distributed fiber optic sensors [7], [8], [9]. Although these methods can effectively suppress noise, they suffer from a degradation of frequency accuracy and spatial resolution, leading to unreliable detection information [9]. Analytical image denoising methods also rely on manual setup and parameter selection. Therefore, deep learning-based image denoising methods have been proposed to overcome these drawbacks. The deep learning denoising methods have shown promising results in suppressing noise while preserving the resolution, making them a viable alternative to analytical methods [10].

The use of the convolutional neural network (CNN) has revolutionized the field of deep learning, particularly in image

Bo Li was with the Department of Engineering, University of Cambridge, CB2 1PZ Cambridge, U.K. She is now with Southeast University, Nanjing 210096, China (e-mail: crystal4315@gmail.com).

Ningjun Jiang is with the Institute of Geotechnical Engineering, Southeast University, Nanjing 210096, China (e-mail: jiangn@seu.edu.cn).

Xiaole Han is with the Department of Civil and Environmental Engineering, University of Hawaii at Manoa, Honolulu, HI 96822 USA (e-mail: xiaole6 @hawaii.edu).
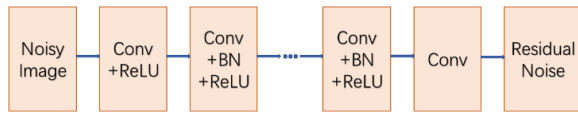
Fig. 1.   DnCNN architecture.

recognition and classification tasks [11]. Compared to the traditional artificial neural network (ANN), the CNN is specifically designed to capture the spatial dependencies in an image by leveraging convolutional layers. The CNN architecture typically consists of an input layer, convolutional layers, pooling layers, one or more fully connected layers, and an output layer [12]. The use of these layers together allows for a more efficient and accurate classification of images. Furthermore, the denoising method of CNN (DnCNN), which uses CNN with residual learning, has shown significant improvement in the performance of image denoising [13]. It learns the noise features, which are easier to learn than clean image features, and predicts the clean image by removing the noise from the noisy input. DnCNN also abandons the pooling layers. This method does not change the redundancy of the information, maintains the same data sampling point number as the input, and does not degrade the frequency accuracy and spatial resolution [14].

We have experimentally demonstrated the denoising performance of DnCNN on small gain SBS STFT-BOTDR by using it on the images of the BGSs along the FUT [14]. The detection of 60 Hz strain vibration is enhanced, with the frequency uncertainty improved by 24%, and the R-squared value of sine fitting of the vibration profile is improved from 0.71 to 0.739. Though the results are better, the improvement of the detection of the sine vibration profile is limited. This might be caused by the lack of time context information during the denoising process. As the vibration is drawn along the time axis, temporal continuity can influence the results. Therefore, in this work, the BGSs are concatenated along the time axis for one spatial location on the FUT to generate the BGS images. The DnCNN is applied to these images, and the experimental results are compared with the results in [14]. Better sinusoidal vibration profiles are detected with the method in this work.

II. PRINCIPLES AND METHODS

A. DnCNN

DnCNN is a convolutional neural network (CNN) architecture designed for image denoising. It is based on the residual learning concept, where the network learns to predict the noise as the residual between the noisy image and the clean image, rather than directly predicting the clean image itself [13]. This approach allows for easier and more efficient learning of the noise pattern.

The DnCNN architecture consists of multiple layers of convolutional filters, batch normalization, and rectified linear units (ReLU) activation functions, as is shown in Fig. 1 [13]. The input to the network is a noisy image, y, which is the sum of a clean image, x, and additive white Gaussian noise, v. The goal of the network is to learn the noise, v, and subtract it from the
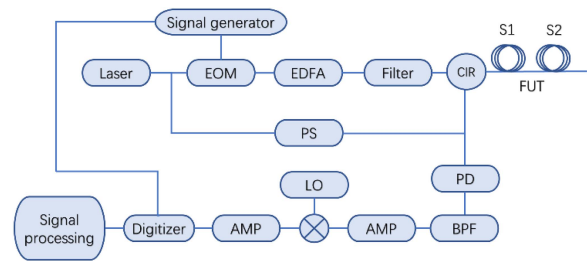

Fig. 2.   Diagram of BOTDR setup.

input image to obtain the clean image, x. The network is trained using a mean squared error (MSE) loss function to minimize the difference between the predicted residual and the actual noise.

The first layer of the DnCNN architecture is a convolutional layer with ReLU activation, which is used to extract low-level features from the noisy image. The ReLU activation function is applied to the output of this layer to introduce nonlinearity and improve the network's ability to learn complex patterns [15]. The subsequent layers consist of convolutional filters with batch normalization and ReLU activation, which are used to extract higher-level features. Batch normalization is used to normalize the output of the previous layer, which helps to stabilize the learning process and improve the performance of the network [16]. The final layer of the network is another convolutional filter, which is used to reconstruct the output image. The denoised image is obtained by subtracting the predicted noise residual from the noisy input image.

Overall, the DnCNN architecture has shown superior performance in image denoising compared to traditional methods, especially for images with high levels of noise. Its ability to learn the noise pattern directly from the data makes it a powerful tool for image denoising applications.

B. BOTDR Setup and Network Training

The experimental setup of STFT-BOTDR for dynamic strain measurement of the fiber under test (FUT) utilizing small gain stimulated Brillouin scattering (SBS) is shown in Fig. 2 [6]. A continuous-wave (CW) laser source is equally split into two arms. The upper arm is modulated by an electro-optic modulator (EOM) with a signal generator to produce a 40ns pulse with a 16μs period, leading to 4 m spatial resolution. The modulated light then passes through an erbium-doped fiber amplifier (EDFA) and an optical bandpass filter for signal amplification and noise reduction, respectively. Then, the incident light is transmitted into the FUT through a circulator (CIR), with the peak pulse power of 3.12 W [6]. Small gain SBS is induced on the FUT by properly setting the output power from the EDFA. The backscattered light from the FUT passes through the circulator again and travels into a 20GHz-bandwidth photodetector (PD). The lower arm, equipped with a polarization scrambler (PS), is directed to the photodetector (PD), as the optical local oscillator. The optical Brillouin signal is converted into an electrical signal on the PD. The electrical signal is then passed through an electrical bandpass filter (BPF), an amplifier (AMP), and down-converted using a 10.5 GHz electrical local
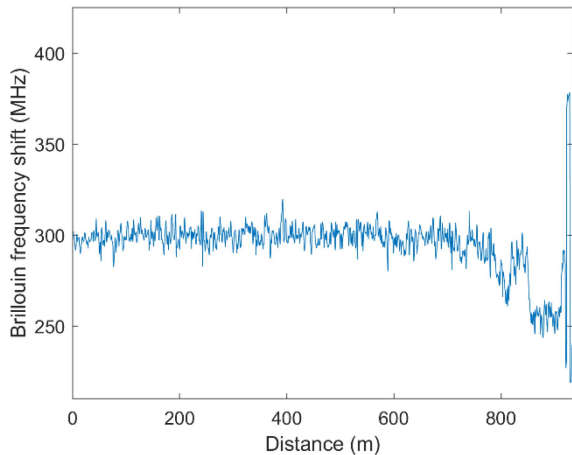
Fig. 3.   Measured BFS distribution over FUT.

oscillator (LO). The resulting signal is amplified again using another amplifier (AMP) and captured by a digitizer of 500 MHz bandwidth. The captured signal is then processed with STFT to obtain Brillouin information. The FUT is approximately 935 m long, with a 60 Hz strain vibration added close to the far end of the fiber over a length of about 6m. The loose fiber section of first 921 m in length is denoted as S1, while the 6 m fiber section with added strain is labeled as S2. There is about 8 m loose fiber after S2, before the end of FUT. The strain vibration is added onto the fiber section S2 through a shaker. The shaker is controlled by an Agilent 33522A to generate 60 Hz sinusoidal displacement along the optic fiber, which leads to sinusoidal strain change. Pre-strain is added on S2 by pulling the optic fiber so that fiber section S2 can be clearly distinguished from the other parts of FUT. Each measurement is obtained after 25 averaging, resulting in a dynamic detection sampling speed of 2.5 kHz. The measured BFS distribution along the FUT is shown in Fig. 3. Fluctuation of the measured BFS along the FUT can be observed. The measured BFS jumps at the end of the profile due to the applied pre-strain on S2.

The measurement with strain vibration lasts for 50ms, leading to about 3 sinusoidal vibration periods, which includes 124 BFS measurements over the FUT. Normally, the BGSs are aligned over the fibre length and the BFS profiles are detected along the FUT. To find the BFS information over time, the BFS for a specific location can be concatenated after found from the BFS profiles over FUT [14]. In this study, to include the time context in the denoising procedure, the 124 BGSs for one location on the FUT are concatenated over time, the BGS image is then denoised by DnCNN, and the BFS information is obtained for this location directly. The BFS profile represents the strain level of the FUT.

For most known distributed fiber optic sensors, the signal distributions are measured along the optic fiber [1], [2], [3], [4], [5]. Commonly, the image denoising methods (e.g., NLM, WD, and BM3D) are also used based on the information along the optic fiber [7], [8], [9]. The kernels act on the images of the spectral information along the fiber length so that the adjacent spatial points are considered during the denoising process. But as each image is independent, time information is not included for the denoising process. And as is discussed in [14], these methods are mainly focused on static measurements, and time context information is not considered.

Our previous work also applies DnCNN on the images of the BGS along the fiber length so that only spatial context information is included but not the time context information [14]. The kernel of CNN moves across the whole image and convolves with the pixels of the same size as the kernel to generate an output. With more than one layer, an output pixel can relate to much more input pixels (the receptive field) than the size of the kernel. Since the time related information is not denoised, the obtained vibration profiles in [14] are not significantly enhanced although the frequency uncertainties are improved. In this study, the kernels work on the images of the BGS for the same location on the optic fiber over time. In this way, a denoised output is connected to the vibration signals over time and the vibration profiles can be better denoised.

To train the DnCNN, the BSDS300 dataset of clean images is used as the training targets [14]. Gaussian noise is then added to these images with a standard deviation of 110 to generate the noisy input images. Thanks to the fact that the target of the network is the residual noise but not the clean images, the BSDS300 dataset is chosen for its greater variability compared to simulated BGS images, which can lead to better training of the network. If there was enough experimental data, real experimental data could also be considered as the training dataset.

Zero padding with padding parameter of 1 and kernel size of 3 are used in this study [17], [18]. The batch size is set to 4. The first convolutional layer with ReLU produces 64 feature maps using 64 filters of size 3 by 3. The middle of the network contains D convolutional layers with BN and ReLU, with each layer using 64 filters of size 3 by 3 by 64. The last convolutional layer is used to reconstruct the output using a single filter of size 3 by 3 by 64. The total depth of (D+2) is to be experimentally studied. The neural network is trained 8 times separately with varying total depths of hidden layers, including 4, 8, 12, and 16, and epoch numbers of 50 and 200. For a sensing point on the FUT, the image of 124 BGSs along the time axis is denoised by each trained network. The BFS over time for this sensing point is extracted from the denoised BGS image.

III. EXPERIMENTAL RESULTS

The BGS images along the time axis are utilized as the input of the DnCNN instead of the BGS images along the fibre length, to include the time context information during the denoising process. The BGS image without DnCNN is shown in Fig. 4(a). The DnCNN denoised BGS image along the time axis for the optic fibre with vibration, with the total depth of 8 and 200 epochs is demonstrated in Fig. 4(b). The center yellow parts of the figures are the BGSs. Sinusoidal changes of the BGS frequencies due to the added strain vibration over time can be observed from the figures. The BGS image without DnCNN is fuzzier. Clearer and smoother sinusoidal shapes after denoising can be observed from Fig. 4(b).
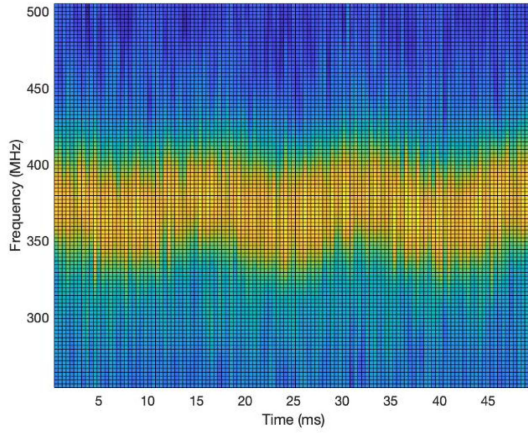
(a) BGS image without denoising
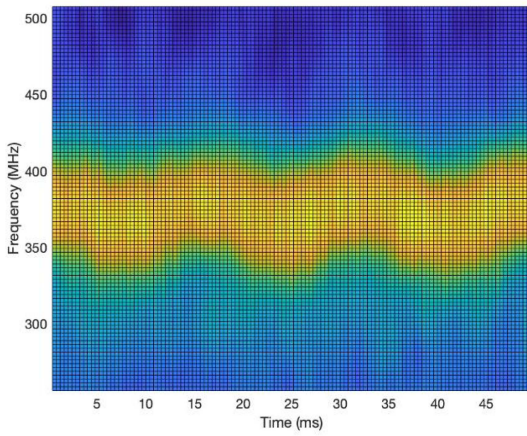
(b) Denoised BGS image with total depth=8, epoch=200

Fig. 4. BGS images along the time axis: (a) without denoising; (b) with denoising, total depth = 8, epoch = 200.

By finding the center frequencies of the denoised BGSs in the images, the vibration profiles are obtained and shown in Fig. 5(a)–(d) with different total depths and epoch numbers of DnCNN. The strain vibration profile without noise reduction is shown in the figures as well.

It can be clearly observed that the derived vibration profiles are smoother with denoising compared with that without denoising. In general, the vibration profiles are more sinusoidal with deeper networks and the larger epoch number. Moreover, it is observed that the detected curves at the troughs and the crests are more fluctuant and harder to be reconstructed. The troughs and the crests are better recovered with deeper layers and more epochs. The total depths of 8, 12 and 16 with 200 epochs lead to better sinusoidal detection of the vibration. Furthermore, by the noise suppression of the BGS images along the time axis instead of along the length of the FUT, the detected vibration profiles are stabler and more sinusoidal. This can be observed by comparing the results in Fig. 4 and the results in [14]. The results in [14] are based on the BGSs along the fibre length, and hence no time information is considered during the denoising and detection
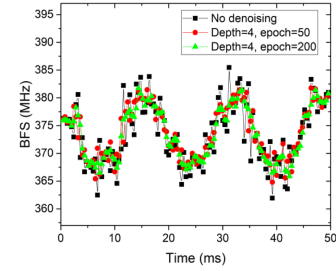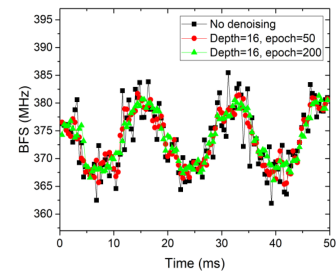

(a) Measured vibration without denoising (black); with DnCNN total depth=4, epoch=50 (red); and with DnCNN total depth=4, epoch=200 (green)
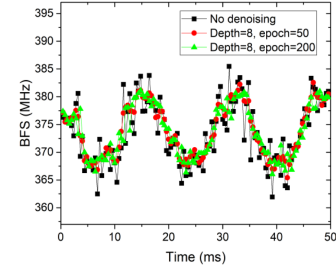
(b) Measured vibration without denoising (black); with DnCNN total depth=8, epoch=50 (red); and with DnCNN total depth=8, epoch=200 (green)
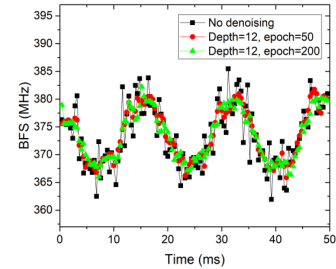
(c) Measured vibration without denoising (black); with DnCNN total depth=12, epoch=50 (red); and with DnCNN total depth=12, epoch=200 (green)

(d) Measured vibration without denoising (black); with DnCNN total depth=16, epoch=50 (red); and with DnCNN total depth=16, epoch=200 (green)

Fig. 5. Strain vibration profiles with and without denoising.

process. On the contrary, by concatenating the BGSs over time in this study, the time context information is included, and better consistency is maintained during the denoising process.

Fig. 6 demonstrates the Brillouin gain spectra of the detected vibration after denoising with different total depths. The suppression of fluctuation can be observed with denoising. The peak positions of the spectra are slightly shifting with different total
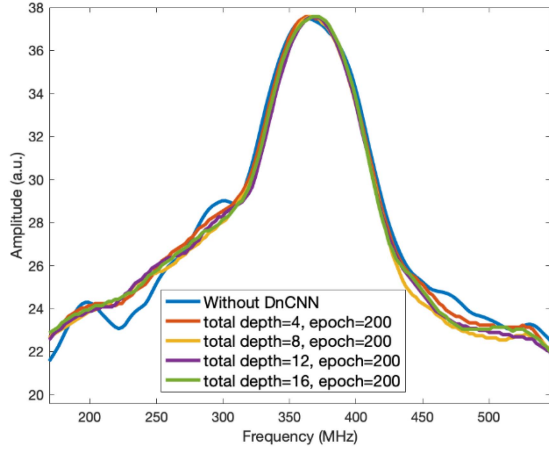
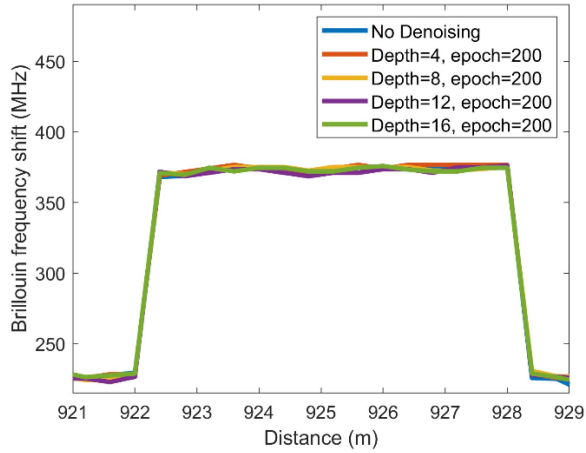Fig. 6. Brillouin gain spectra with different depths of network.

Fig. 7. BFS profiles of the fiber section S2.

TABLE I
SINE FITTING R-SQUARED VALUES OF THE VIBRATION PROFILES WITH
DIFFERENT DEPTHS AND EPOCHS

No.	Depth	Epoch number	R-squared value	
			BGSs along FUT [14]	BGSs over time
a	4	50	0.724	0.871
b	4	200	0.719	0.89
c	8	50	0.728	0.906
d	8	200	0.739	0.907
e	12	50	0.721	0.914
f	12	200	0.731	0.931
g	16	50	0.714	0.882
h	16	200	0.73	0.923
i	-	-	0.71	0.71

values are derived for each total depth and epoch number and listed in Table I. The R-squared values with the denoising of BGS images along the fibre length in [14] are also listed as a comparison. No. i in Table I is the value without denoising.

From Table I, it can be observed that the R-squared values are well enhanced by noise reduction of the BGS images along the time axis, compared with the original result and the results with denoising along the fibre length, benefiting from the introduction of the time context information. With 200 epochs, the derived R-squared values reach 0.907 with 8 layers, 0.931 with 12 layers and 0.923 with 16 layers respectively, demonstrating a good correlation with the added strain vibration of sinewave.

Moreover, with the denoising conducted on the BGS images along the time axis, larger R-squared values are obtained with 200 epochs compared with those with 50 epochs, when the depths of the network are the same. Besides, when the epoch number is fixed, the R-squared values increase as the total depth gets larger from 4, 8, to 12. When the total depth is 16, the R-squared values decrease compared with those with total depth of 12. In this situation, a high R-squared value is still obtained with 200 epochs, although the value is slightly lower than that with 12 layers. But with 50 epochs, the R-squared with 16 layers is only comparable with the values with 4 layers.

B. The Frequency Uncertainties and SNR

The frequency uncertainties of the BFS are then calculated for each total depth and epoch number and listed in Table II, with the original value without denoising given as No. i of the table as a comparison. The values are compared with the frequency uncertainties obtained based on the denoising of BGS images along the FUT in [14].

As is found in Table II, the best frequency uncertainties of 2.32 MHz and 2.38 MHz are obtained with the total depths of 8 and 16 when the epoch number is 200, leading to the improvement of 2.78 MHz and 2.72 MHz respectively from

depths, indicating fluctuant denoising results by the change of the depths. With each setting, the network is trained independently. For different depths, the number of trainable parameters are different. Besides, the trainable parameters are fine-tuned as the loss function is minimized with different depths. The parameters of the trained networks are hence different, so that the predicted noise cannot be exactly the same as well as the output clean images. As a result, the denoised spectra and their peak positions can subtly vary.

Fig. 7 is the derived BFS profiles along the optic fiber with different settings of total depths and epoch numbers for fiber section S2. The strain applied onto the optic fiber can be detected after denoising. It can be seen that the 10% to 90% of the rising edge (the transition region of the BFS from the low value to the high value) is not degraded with DnCNN, which defines the spatial performance of a distributed fiber optic sensor.

IV. DISCUSSION

A. The Sine Fitting R-squared Values

The detected vibration profiles are sine fitted to numerically verify the denoising performance. The sine fitting R-squared

TABLE II
FREQUENCY UNCERTAINTIES OF BFS WITH DIFFERENT DEPTHS AND
EPOCH NUMBERS

No.	Depth	Epoch number	Frequency uncertainty (MHz)	
			BGSs along FUT [14]	BGSs over time
a	4	50	4.93	3.33
b	4	200	4.42	2.78
c	8	50	4.01	2.36
d	8	200	3.88	2.32
e	12	50	4.56	2.83
f	12	200	4.23	2.51
g	16	50	4.31	2.60
h	16	200	3.62	2.38
i	-	-	5.1	5.1

TABLE III
FREQUENCY UNCERTAINTIES, R-SQUARED VALUES, AND SNR FOR DIFFERENT
EPOCH NUMBERS, WITH TOTAL DEPTH OF 8

Epoch number	Frequency uncertainty (MHz)	R-squared value	SNR
50	2.36	0.906	9.38
100	2.38	0.906	9.36
200	2.32	0.907	9.64
300	2.29	0.909	9.69

denoising. But by aligning the BGSs along the time axis for denoising, the SNR values are better enhanced, compared to the SNR values when the images of the BGSs along the FUT are utilized. The enhancement of SNR in Fig. 8 matches the trends of the uncertainty improvement in Table II.

As a matter of fact, similar to the results by denoising of the BGS images along the FUT, the frequency uncertainties are better suppressed as the total depth gets greater from 4 to 8, and then rebound a little bit as the total depth increases to 12, then reduce again when the total depth is 16. The fluctuant frequency uncertainties and the R-squared values, as the depth of the network gets deeper, can be attributed to the progressive extraction of higher-level features in the network, where each layer captures increasingly complex characteristics of the input. When utilizing a shallower network with 4 layers, the DnCNN primarily extracts lower-level features and fails to acquire sufficient discriminative information from the target BGS images. However, as the network depth increases to 8, more intricate features are captured, leading to superior denoising performance. The trend becomes less favorable as the total depth reaches 12 or 16. Although the deeper network can extract even more complex features, it can also introduce a larger number of trainable parameters, resulting in a more challenging training process. In addition, BGS images differ from typical natural images, as they consist of numerous spectra with similar features and less intricate characteristics. Deeper networks might lead to higher risks of image overfitting, and details may be concealed [8], [14]. The R-squared values and the frequency uncertainties are comparable with the depths of 8 and 16. Therefore, since 8 layers can produce good denoised results and more layers can generate fluctuant results in terms of uncertainties and R-squared values, the total depth of 8 is the most feasible choice for this work.

Fig. 8. SNR by using DnCNN with different depths and epoch numbers.

C. Comparison of Different Epoch Numbers

The frequency uncertainties, R-squared values, and SNR, with different epoch numbers when total depth is 8, are given in Table III. Fig. 9 shows the training loss curve when depth is 8 and epoch number is 300.

As the epoch number increases, the frequency uncertainty, the R-squared value, and the SNR all tend to become better. When epoch number is 50, the results are subtly better than those with epoch number of 100, and the results are only slightly worse than those with epoch number of 200. But by comparing all the results in Table I and II, apart from the values for total depth of 8, all other results show more obvious improvement when the epoch number is increased from 50 to 200. Therefore, the results

the original value. That is to say, the frequency uncertainty is halved after denoising. With 12 total depth and 200 epochs, the frequency uncertainty obtained is 2.51 MHz, which is also around half of the original value with the reduction of 2.59 MHz. Furthermore, the obtained frequency uncertainties are well enhanced compared with the values by the denoising of the BGSs along the FUT, with a difference of 1.56 MHz at the total depth of 8 and epoch number of 200 and a difference of 1.24 MHz at the total depth of 16 and epoch number of 200. This is due to the fact that the frequency uncertainty is calculated as the standard deviation of BFS over time and that the BFS information along the time axis is better acquired as the time context information is considered for denoising.

The SNR for different depths and epoch numbers in this work, as well as the SNR of the results of our previous work [14] and the SNR without denoising are compared in Fig. 8. The SNR is improved within the range of 2.22dB (depth = 4, epoch = 50) to 3.67dB (depth = 8, epoch = 200) by using DnCNN on the images of BGSs over time, compared to the SNR without denoising. By using DnCNN on the images of BGSs along the optic fiber, the SNR is also improved compared to that with no
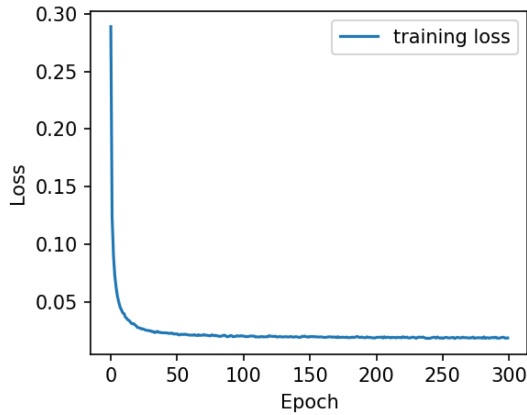
Fig. 9.   Loss curve for total depth = 8, epoch = 300.

with total depth of 8 and epoch number of 50 here can be due to a single good training of the network.

From Fig. 9, it can be observed that the loss curve tends to become stable with 50 epochs. For image denoising of natural pictures with CNN, epoch number of 50 can be used to generate reasonable outputs [13]. Besides, the loss function is already well converged when the epoch number is 200. By increasing the epoch number to a greater value, the denoising performance on BOTDR can be improved, but the improvement can be limited. Therefore, the epoch number of 200 can lead to well denoised results, but the epoch number can be set to even larger value if extreme results are desired, with more time consumption.

Conclusively, the frequency uncertainties and the R-squared values obtained by DnCNN denoising of the BGS images along the time axis are better, compared with the values by denoising of the BGS images along the FUT. The network with 8 layers and 200 epochs can lead to well denoised results, with the frequency uncertainty of 2.32 MHz and R-squared value of 0.907. Moreover, if there are enough experimental data, real noisy dataset could be used as the training set of the networks. In addition, it is worthy of noticing that the spatial context information is missing by concatenating the BGSs along the time axis. So, the denoising of the BGS images along the time axis can result in better detection of the strain vibration over time whereas the denoising of the BGS images along the fibre length can better maintain the spatial correlation of the sampling points along the FUT. Depending on the application of the BOTDR system, proper BGS images should be chosen.

Currently, the commonly used image denoising methods for Brillouin based sensors are NLM, WD, and BM3D. These methods show significant improvement of the BFS uncertainty but can also hugely degrade the performance in terms of frequency accuracy and spatial resolution [7], [8], [9], [19]. Frequency degradation of as large as 23 times of the nominal frequency uncertainty has been demonstrated, which makes the measurement untrustworthy [9]. In addition, parameter adjustment has a significant influence on the denoising performance, and the accuracy of NLM relies on the similarity of neighboring data. Besides, many published works calculate the frequency

uncertainty as the standard deviation of BFS along the FUT within a certain length, which overestimates the uncertainty to smaller values. Standard deviation over time has been proved to be the more accurate calculation [19]. In this work, standard deviation over time is applied. The confusion of the definition of frequency uncertainty makes the comparison difficult. Furthermore, due to the different settings of spatial resolution, averaging number, data acquisition method, and the different setups of Brillouin-based sensors (BOTDA or BOTDR), it is even more difficult to compare the denoising performance. On the other hand, most of the known denoising methods are applied to static measurements, while this work uses DnCNN on the vibration measurement. According to Nyquist theorem, with a sampling rate of 2.5 kHz, vibration of up to 1.25 kHz can be measured with the setup of small gain SBS STFT-BOTDR in this work.

V. CONCLUSION

BOTDR is a sensing technique that can be used to detect changes in strain and temperature along a fiber optic cable. Dynamic measurement using small gain SBS STFT-BOTDR has promising applications but the system performance is limited by the existing noise and the small number of averaging. The BGS images obtained from the captured time domain data can be denoised to improve the BFS signals and the accuracy of the measurements. Image denoising methods such as NLM, WD, and BM3D have been shown to improve BFS uncertainty, but may also lead to significant degradation of frequency accuracy and spatial resolution. Besides, for many known publications regarding the image denoising of the Brillouin scattering based distributed fiber optic sensors, the frequency uncertainty is calculated as the standard deviation of BFS along the FUT. The uncertainties are estimated to smaller values and inaccurate with this method, compared to the method of calculating the frequency uncertainty as the standard deviation over time. In this work, the standard deviation over time is adopted to calculate the frequency uncertainties, so that the results are more accurate.

The image denoising method of DnCNN is applied to the BGS images along the time axis in this work, for the strain vibration detection of the small gain SBS STFT-BOTDR system. Significant improvement is demonstrated in terms of frequency uncertainty and R-squared value with the denoising of BGS images along the time axis, compared to the denoising along the FUT. The frequency uncertainty is reduced from 3.88 MHz to 2.32 MHz, and the R-squared value is increased from 0.739 to 0.907. Compared to the original value without denoising, with a total depth of 8 and an epoch number of 200, the frequency uncertainty is improved to 45% of the original value, from 5.1 MHz to 2.32 MHz, and the R-squared value is enhanced from 0.71 to 0.907. By denoising of the BGS images along the time axis, the strain vibration profiles are better recovered and more sinusoidal, as the time context information is considered during the denoising process. Consequently, effective noise reduction and improved vibration detection is realised with BGS image denoising along the time axis.

REFERENCES

[1] F. Bastianini, R. Di Sante, F. Falcetelli, D. Marini, and G. Bolognini, "Optical fiber sensing cables for Brillouin-based distributed measurements," *Sensors*, vol. 19, no. 23, Nov. 2019, Art. no. 5172.

[2] A. Barrias, J. R. Casas, and S. Villalba, "A review of distributed optical fiber sensors for civil engineering applications," *Sensors*, vol. 16, no. 5, May 2016, Art. no. 748.

[3] B. Yuan, Y. Ying, M. Morgese, and F. Ansari, "Theoretical and experimental studies of micro-surface crack detections based on BOTDA," *Sensors*, vol. 22, no. 9, May 2022, Art. no. 3529.

[4] Y. Muanenda, C. J. Oton, and F. Di Pasquale, "Application of Raman and Brillouin scattering phenomena in distributed optical fiber sensing," *Front. Phys.*, vol. 7, Oct. 2019, Art. no. 155.

[5] K. Kishida, M. Imai, J. Kawabata, and A. Guzik, "Distributed optical fiber sensors for monitoring of civil engineering structures," *Sensors*, vol. 22, no. 12, Jun. 2022, Art. no. 4368.

[6] B. Li, L. Luo, Y. Yu, K. Soga, and J. Yan, "Dynamic strain measurement using small gain stimulated Brillouin scattering in STFT-BOTDR," *IEEE Sensors J.*, vol. 17, no. 9, pp. 2718–2724, May 2017.

[7] M. A. Soto, J. Z. Ramírez, and L. Thévenaz, "Intensifying the response of distributed optical fibre sensors using 2D and 3D image restoration," *Nature Commun.*, vol. 7, Mar. 2016, Art. no. 10870.

[8] S. Zaslawski, Z. Yang, and L. Thévenaz, "On the 2D post-processing of Brillouin optical time-domain analysis," *J. Lightw. Technol.*, vol. 38, no. 14, pp. 3723–3736, Jul. 2020.

[9] H. Wu, L. Wang, Z. Zhao, N. Guo, C. Shu, and C. Lu, "Brillouin optical time domain analyzer sensors assisted by advanced image denoising techniques," *Opt. Exp.*, vol. 26, no. 5, pp. 5126–5139, 2018.

[10] C. Tian, L. Fei, W. Zheng, Y. Xu, W. Zuo, and C. Lin, "Deep learning on image denoising: An overview," *Neural Netw.*, vol. 131, pp. 251–275, Nov. 2020.

[11] E. Frank, Y. Zhen, F. Han, T. Shailesh, and D. Matthias, "An introductory review of deep learning for prediction models with Big Data," *Front. Artif. Intell.*, vol. 3, Feb. 2020, Art. no. 4.

[12] I. Goodfellow, Y. Bengio, and A. Courville, *Deep Learning*. Cambridge, MA, USA: MIT Press, 2016.

[13] K. Zhang, W. Zuo, Y. Chen, D. Meng, and L. Zhang, "Beyond a Gaussian denoiser: Residual learning of deep CNN for image denoising," *IEEE Trans. Image Process*, vol. 26, no. 7, pp. 3142–3155, Jul. 2017.

[14] B. Li, N. Jiang, and X. Han, "Denoising of BOTDR dynamic strain measurement using convolutional neural networks," *Sensors*, vol. 23, no. 4, Feb. 2023, Art. no. 1764.

[15] H. Ide and T. Kurita, "Improvement of learning for CNN with ReLU activation by sparse regularization," in *Proc. Int. Joint Conf. Neural Netw.*, Anchorage, AK, USA, 2017, pp. 2684–2691.

[16] S. Ioffe and C. Szegedy, "Batch normalization: Accelerating deep network training by reducing internal covariate shift," in *Proc. 32nd Int. Conf. Mach. Learn.*, 2015, pp. 448–456.

[17] V. Dumoulin and F. Visin, "A guide to convolution arithmetic for deep learning," Mar. 2016, *arXiv:1603.07285*.

[18] X. Li, F. Li, X. Fern, and R. Raich, "Filter shaping for convolutional neural networks," in *Proc. 5th Int. Conf. Learn. Representations*, Apr. 24–26, 2017, pp. 1–7.

[19] M. A. Soto, Z. Yang, J. A. Ramírez, S. Zaslawski, and L. Thévenaz, "Evaluating measurement uncertainty in Brillouin distributed optical fibre sensors using image denoising," *Nature Commun.*, vol. 12, Aug. 2021, Art. no. 4901.